Letters

A Multichannel High-Current AGV Wireless Charging System Based on Perpendicular DD Coil Array and Current Multiplier Rectifier

Yiming Zhang, *Senior Member, IEEE*, Hongjing Ouyang, Yizhan Zhuang, Xiangpeng Cheng, Xiaoying Chen, and Xingkui Mao

***Abstract*—With the rapid development of wireless power transfer (WPT) technology, high-power wireless charging for the automatic guided vehicle (AGV) has become a hot topic in recent years. The charging voltage of the AGV is lower than 60 V, the receiver current can be tens of amperes, forming a low-voltage high-current system. In this article, an *N*-channel interleaved current-multiplier WPT system is proposed to promote the current level as well as the system reliability. The perpendicular double D coil array with self-decoupling is adopted to realize independent power transmission of each channel. Finally, a four-channel current-quadruple WPT prototype is built and a series of experiments are conducted. The results show that the system reaches an output power of about 2 kW with the efficiency of 87.81%.**

***Index Terms*—Automatic guided vehicle (AGV), current multiplier rectifier, high-current output, multichannel, wireless power transfer (WPT).**

I. Introduction

WIRELESS power transfer (WPT) technology [1], [2], [3], [4] adopts noncontact charging mode, which avoids the danger of sparks and electric shock during plugging in and out, and ensures the safety of personnel and equipment [5], [6], [7], [8]. It has become the cornerstone of the automatic guided vehicle (AGV) in industrial automation. To reduce the charging time, the charging power is continuously improved. Since the charging voltage of the AGV is lower than 60 V with typical voltages of 48, 24, and 12 V, the receiver current is at least tens of amperes, forming a low-voltage high-current (LVHC) system [9], [10], [11], [12].

For the LVHC-WPT system, the main challenge is the high rating requirements and high conduction loss of devices. To solve this challenge, a dual-channel paralleling WPT system based on bilateral coil decoupling was proposed in [13], which reduces the current on each channel and improves the stability of the system without affecting the power. The double D (DD) coil was horizontally stacked on the ferrite, and the solenoid coil was nested and wound on the DD coil and ferrite, eliminating additional cross coupling, and the coil was compact. The expansion of number of paralleling channels is limited due to the use of vertical magnetic field to realize coil decoupling, and the devices still face challenges when facing higher transmission power.

To face higher power, scalable multichannel paralleling WPT systems have become the preferred solution. A multiphase interleaved WPT system was proposed in [14], with an interleaved control strategy to an N-phase system of a phase shift of π/N, reducing output current ripples. In [15], a three-loop strategy is adopted to realize power balance among the multiple channels. For the aforementioned method, the number of paralleling channels is unlimited and can be expanded as required. With the increase of number of paralleling channels, the transmission power also increases.

In addition to using the multichannel paralleling system, the current doubler rectifier (CDR) is also commonly used for high-current output. A current doubler synchronous rectifier instead of a traditional full-bridge rectifier was proposed in [16], utilizing the energy storage characteristics of inductors during the cycle to achieve multiple current pulses and improve the output current. Adding additional inductors changes the original resonance relationship, so parallel compensation is adopted, resulting in the system being sensitive to parameter changes and experiencing significant transient response shocks.

To solve the problem of changing the output characteristics of energy storage inductors, introducing negative coupling between energy storage inductors was proposed in [17], which has output characteristics similar to the full-bridge rectifier and can be compensated in series, with strong applicability.

Combining the advantages of two existing high-current output methods, this article proposes an N-channel interleaved WPT system with a current multiplier rectifier (CMR), where the number of paralleling channels can increase with the power level demand without limitation, and the input characteristics are similar to full-bridge rectifier. The main contributions of this article are as follows.

1) On the basis of the dual-channel CDR, the design principle of the system is elaborated and extended, and a general

Received 4 June 2025; revised 1 August 2025 and 2 September 2025; accepted 20 September 2025. Date of publication 29 September 2025; date of current version 13 November 2025. This work was supported by the National Natural Science Foundation of China under Grant 52577187 and Grant 52407197. *(Corresponding authors: Xiangpeng Cheng; Xiaoying Chen.)*

The authors are with the School of Electrical Engineering and Automation, Fuzhou University, Fuzhou 350108, China (e-mail: zym@fzu.edu.cn; 230120038@fzu.edu.cn; zyz_joe@fzu.edu.cn; cxp@fzu.edu.cn; fzucxy@fzu.edu.cn; mxk782@fzu.edu.cn).

Color versions of one or more figures in this article are available at https://doi.org/10.1109/TPEL.2025.3614467.

Digital Object Identifier 10.1109/TPEL.2025.3614467

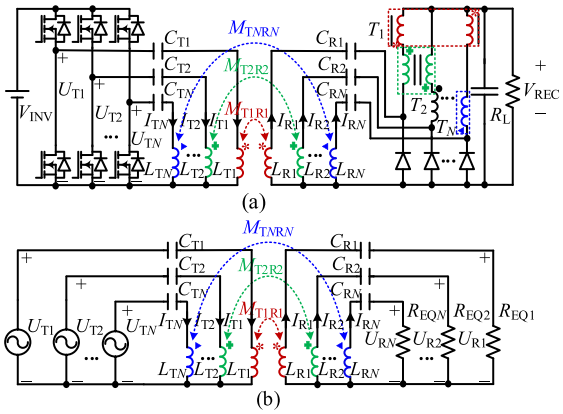

Fig. 1. Proposed N-channel interleaved CMR. (a) Topology. (b) Equivalent circuit.

mathematical model of the N-channel CMR is established. Without altering the resonance relationship and system characteristics, the CMR achieves higher step-down from input to output.

2) By adopting a control strategy of interleaved conduction, the output of the rectifier is not merely the simple parallel superposition of currents, but instead, the maximum current at any given moment is selected for superimposed output, which can effectively increase the current gain.
3) A perpendicular DD coil array structure is proposed, which realizes the cross-coupling between nonpositive coils through perpendicular magnetic field distribution, effectively eliminates the power coupling problem caused by cross-inductance, and is flexible and free in the expansion direction.
4) The proposed multichannel system can be added on the basis of the original system when expanding the new channel, avoiding redesign, and has the characteristics of high system compatibility.

The rest of this article is organized as follows. Section II details the N-channel interleaved CMR topology. Section III presents the magnetic coupling structure. In Section IV, a four-channel prototype is constructed and experiments are carried out to verify the proposed control strategy. Finally, Section V concludes this article.

II. Proposed High-Current Output Method

To avoid confusion in variable naming, the following variable naming formats are explained. For vectors under ac equivalent circuits, they are uniformly capitalized and bolded. The constant scalar in the rest of the dc circuit is indicated only in uppercase, and lowercase variables indicate that it will change over time.

A. Topology and Modeling

The proposed N-channel interleaved CMR topology and equivalent circuit are shown in Fig. 1(a) and (b). The interleaved control strategy is applied in different legs with a phase shift of $2\pi/N$. V_{INV} and $U_{\mathrm{T}i}$ are the inverter dc voltage and fundamental ac voltage of the channel i, respectively. They can be expressed as

$$\boldsymbol{U_{\mathrm{T}i}} = \frac{\sqrt{2}V_{\mathrm{INV}}}{\pi}. \tag{1}$$

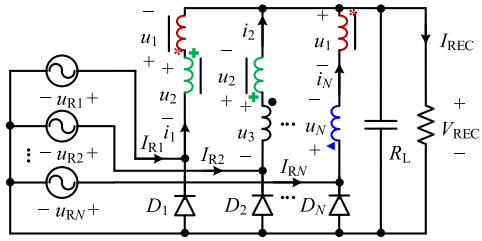

Fig. 2. Rx equivalent circuit.

$L_{\mathrm{T}i}$ ($L_{\mathrm{R}i}$) and $I_{\mathrm{T}i}$ ($I_{\mathrm{R}i}$) are defined as the self-inductance and current of the transmitting (Tx) (receiving, Rx) coil of the Channel i. $C_{\mathrm{T}i}$ and $C_{\mathrm{R}i}$ are the compensation capacitors. In the proposed topology, only couplings between coil pairs are considered, which are defined as $M_{\mathrm{T1R1}}, M_{\mathrm{T2R2}}, \ldots, M_{\mathrm{T}N\mathrm{R}N}$, and the other cross couplings are neglected.

Assume the parameters of each channel are identical, namely

$$\begin{cases} M_{\mathrm{T1R1}} = M_{\mathrm{T2R2}} = \cdots = M_{\mathrm{T}N\mathrm{R}N} = M_{\mathrm{TR}} \\ R_{\mathrm{EQ1}} = R_{\mathrm{TEQ2}} = \cdots = R_{\mathrm{EQ}N} = R_{\mathrm{EQ}} \end{cases}. \tag{2}$$

The system works at the resonant angular frequency ω

$$\omega = \frac{1}{\sqrt{L_{\mathrm{T}i}C_{\mathrm{T}i}}} = \frac{1}{\sqrt{L_{\mathrm{R}i}C_{\mathrm{R}i}}}. \tag{3}$$

Using Kirchhoff's voltage law (KVL) and ignoring the Equivalent Series Resistances, one can get

$$\begin{cases} \boldsymbol{U_{\mathrm{T}i}} = \left(\mathrm{j}\omega L_{\mathrm{T}i} + \frac{1}{\mathrm{j}\omega C_{\mathrm{T}i}}\right)\boldsymbol{I_{\mathrm{T}i}} - \mathrm{j}\omega M_{\mathrm{TR}}\boldsymbol{I_{\mathrm{R}i}} \\ \mathrm{j}\omega M_{\mathrm{TR}}\boldsymbol{I_{\mathrm{T}i}} = \left(\mathrm{j}\omega L_{\mathrm{R}i} + \frac{1}{\mathrm{j}\omega C_{\mathrm{R}i}} + R_{\mathrm{EQ}}\right)\boldsymbol{I_{\mathrm{R}i}} \end{cases}. \tag{4}$$

Correspondingly, the current in each branch is

$$\boldsymbol{I_{\mathrm{T}i}} = \frac{\boldsymbol{U_{\mathrm{T}i}}R_{\mathrm{EQ}}}{\omega^2 M_{\mathrm{TR}}^2}, \boldsymbol{I_{\mathrm{R}i}} = \frac{\boldsymbol{U_{\mathrm{T}i}}}{\omega M_{\mathrm{TR}}}. \tag{5}$$

B. Current Multiplier Analysis

Based on aforementioned analysis, the Tx can be converted to the Rx as a current source, as shown in Fig. 2.

In Fig. 2, the N-channel CMR is shown, which consists of N transformers and diodes. V_{REC} and R_{L} represent the output voltage and load resistance, respectively. u_i and i_i are the voltage and current on the transformers, respectively.

For equivalent current sources, the voltage at both ends is the highest at the peak current, while the diode in the CMR uses a common anode connection, which is clamped off. As each current source is staggered and continuously feeds the output, the position of the shutdown diode is also shifted at $2\pi/N$, and the corresponding operating modes and key waveforms are shown in Fig. 3.

When $\omega t \in [\pi/2 - \pi/N \sim \pi/2 + \pi/N]$, the CMR operates in Mode 1, D_1 is turned OFF, D_2 to D_N are turned ON. Using the KVL and considering characteristics of the transformer, the

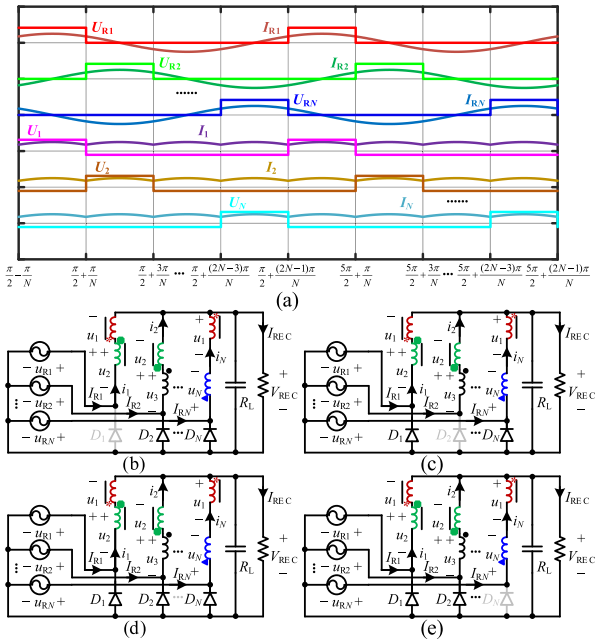

Fig. 3. Working modes. (a) Key waveforms. (b) Mode 1. (c) Mode 2. (d) Mode *i*. (e) Mode *N*.

currents i_i and voltages $u_{\mathrm{R}i}$ (u_i) are expressed as

$$\begin{cases} u_{\mathrm{R1}} = u_1 - u_2 + V_{\mathrm{REC}} \\ u_{\mathrm{R2}} = \cdots = u_{\mathrm{RN}} = 0 \\ u_3 - u_2 = \cdots = u_N - u_{N-1} = u_1 - u_N = V_{\mathrm{REC}} \\ i_1 = \cdots = i_{\mathrm{N}} = \sqrt{2} I_{\mathrm{R1}} \sin(\omega t) \end{cases}. \tag{6}$$

Correspondingly, the voltages u_{R1} of current source and $u_1 - u_2$ of the transformer are derived as

$$\begin{cases} u_{\mathrm{R1}} = N V_{\mathrm{REC}} \\ u_1 - u_2 = (N-1) V_{\mathrm{REC}} \end{cases}. \tag{7}$$

When $\omega t \in [\pi/2 + \pi/N \sim \pi/2 + 3\pi/N]$, the CMR operates in Mode 2, D_2 is turned OFF. The currents i_i and voltages $u_{\mathrm{R}i}$ (u_i) are expressed as

$$\begin{cases} u_{\mathrm{R2}} = u_2 - u_3 + V_{\mathrm{REC}} \\ u_{\mathrm{R2}} = \cdots = u_{\mathrm{RN}} = u_{\mathrm{R1}} = 0 \\ u_4 - u_3 = \cdots = u_N - u_{N-1} = u_1 - u_N = u_2 - u_1 = V_{\mathrm{REC}} \\ i_1 = \cdots = i_{\mathrm{N}} = \sqrt{2} I_{\mathrm{R1}} \sin\left(\omega t - \frac{2\pi}{N}\right) \end{cases}. \tag{8}$$

Similarly, the voltages u_{R2} of current source and $u_2 - u_3$ of the transformer are derived as

$$\begin{cases} u_{\mathrm{R2}} = N V_{\mathrm{REC}} \\ u_2 - u_3 = (N-1) V_{\mathrm{REC}} \end{cases}. \tag{9}$$

When $\omega t \in [\pi/2 + (2N\text{-}3)\pi/N \sim \pi/2 + (2N\text{-}1)\pi/N]$, the CMR operates in Mode N, D_N is turned OFF. The currents i_i and voltages $u_{\mathrm{R}i}$ (u_i) are expressed as

$$\begin{cases} u_{\mathrm{RN}} = u_1 - u_N + V_{\mathrm{REC}} \\ u_{\mathrm{R1}} = \cdots = u_{\mathrm{R}(N-1)} = 0 \\ u_1 - u_2 = \cdots = u_{N-1} - u_N = V_{\mathrm{REC}} \\ i_1 = \cdots = i_{\mathrm{N}} = \sqrt{2} I_{\mathrm{R1}} \sin\left(\omega t - \frac{(N-1)2\pi}{N}\right) \end{cases}. \tag{10}$$

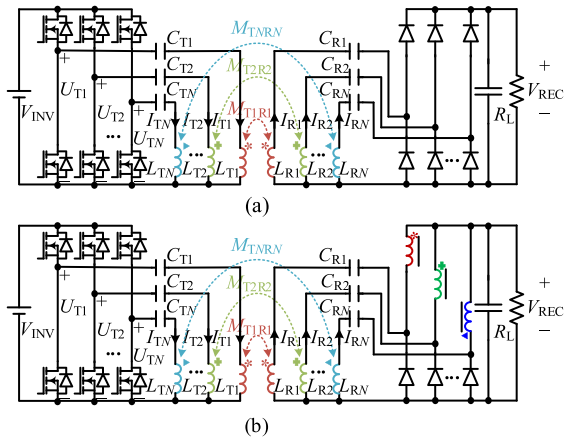

Fig. 4. Traditional *N*-channel interleaved topology. (a) MPR. (b) PCDR.

Based on aforementioned analysis, the voltages $u_{\mathrm{R}N}$ of current source and $u_1 - u_N$ of the transformer are derived as

$$\begin{cases} u_{\mathrm{R}N} = N V_{\mathrm{REC}} \\ u_1 - u_N = (N-1) V_{\mathrm{REC}} \end{cases}. \tag{11}$$

Considering no dc current can pass through capacitance, the dc component of $i_1 + i_2 + \ldots + i_N$ must be equal to the load current I_{REC}. By equating dc components, it is obtained as

$$I_{\mathrm{REC}} = \frac{\sqrt{2}}{2\pi} \int_0^{2\pi} \sum_{i=1}^{N} i_i(\omega t) d(\omega t) = \frac{2 V_{\mathrm{INV}} N^2}{\pi^2 \omega M_{\mathrm{TR}}} \sin\left(\frac{\pi}{N}\right). \tag{12}$$

By Fast Fourier Transform, the fundamental wave component corresponding to $\boldsymbol{U_{\mathrm{R}i}}$ is calculated as

$$\begin{aligned} \boldsymbol{U_{\mathrm{R}i}} &= \frac{1}{2\pi} \int_0^{2\pi} u_{\mathrm{R}i}(\omega t) \sin(\omega t) d(\omega t) \\ &= \frac{2 R_{\mathrm{L}} \boldsymbol{U_{\mathrm{T}i}} N^3}{\pi^2 \omega M_{\mathrm{TR}}} \left(\sin\left(\frac{\pi}{N}\right)\right)^2. \end{aligned} \tag{13}$$

The equivalent resistance of the CMR can be modeled as a pure resistive load R_{EQ} as follows:

$$R_{\mathrm{EQ}} = R_{\mathrm{EQ}i} = \frac{U_{\mathrm{R}i}}{I_{\mathrm{R}i}} = \frac{2 R_{\mathrm{L}}}{\pi^2} N^3 \left(\sin\left(\frac{\pi}{N}\right)\right)^2. \tag{14}$$

C. Comparison With the Traditional High-Current Output Method

To illustrate the advantages of the proposed CMR, the traditional multiphase rectifier (MPR) and parallel current doubler rectifier (PCDR) are compared under the same number of channels and interleaved control. The traditional *N*-channel interleaved MPR and PCDR topologies are shown in Fig. 4(a) and (b), respectively, only the rectifier structure is different compared with Fig. 1(a).

Considering the analysis method and the equivalent circuit of MPR and PCDR are similar to the previous paper, it will not be repeated here. The key parameters of three topologies and current waveforms on each channel of the rectifier are shown in Table I and Fig. 5, respectively.

TABLE I
COMPARISONS OF MPR, PCDR, AND CMR

Rectifier	MPR	PCDR	CMR
I_{T}	$\frac{2\sqrt{2}R_{\mathrm{L}}V_{\mathrm{INV}}}{\pi^3\omega^2M_{\mathrm{TR}}^2}N$	$\frac{2\sqrt{2}R_{\mathrm{L}}V_{\mathrm{INV}}}{\pi^3\omega^2M_{\mathrm{TR}}^2}4N$	$\frac{2\sqrt{2}R_{\mathrm{L}}V_{\mathrm{INV}}}{\pi^3\omega^2M_{\mathrm{TR}}^2}N^3\left(\sin(\frac{\pi}{N})\right)^2$
I_{R}	$\frac{\sqrt{2}V_{\mathrm{INV}}}{\pi\omega M_{\mathrm{TR}}}$	$\frac{\sqrt{2}V_{\mathrm{INV}}}{\pi\omega M_{\mathrm{TR}}}$	$\frac{\sqrt{2}V_{\mathrm{INV}}}{\pi\omega M_{\mathrm{TR}}}$
I_{REC}	$\frac{2V_{\mathrm{INV}}}{\pi^2\omega M_{\mathrm{TR}}}N$	$\frac{2V_{\mathrm{INV}}}{\pi^2\omega M_{\mathrm{TR}}}2N$	$\frac{2V_{\mathrm{INV}}}{\pi^2\omega M_{\mathrm{TR}}}N^2\sin\left(\frac{\pi}{N}\right)$

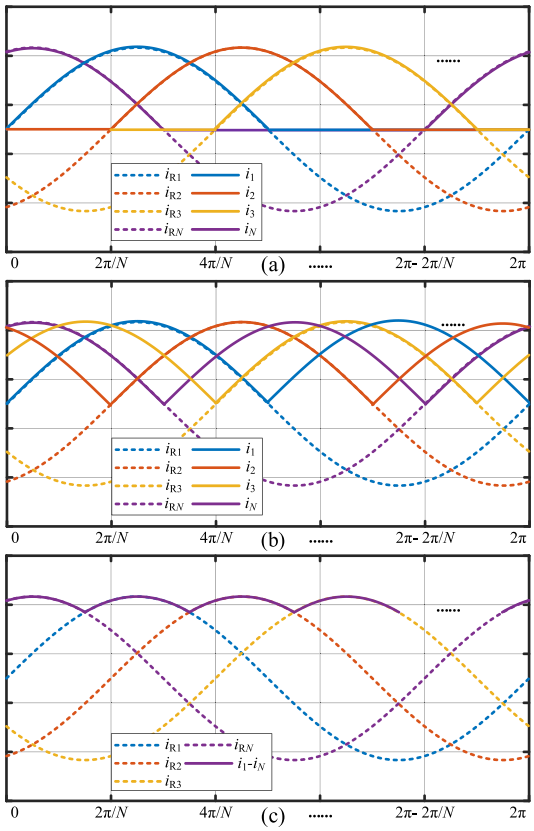

Fig. 5. Current waveforms of Rx and rectifier. (a) MPR. (b) PCDR. (c) CMR.

In Fig. 5(a), the current passing through each channel of the MPR is a half sine wave due to the unidirectional conductivity of diode, maintaining a phase shift of $2\pi/N$ between the different channels, and finally superimposing the outputs. In Fig. 5(b), the freewheeling characteristics of the transformer allow current to pass through each channel of the PCDR as a whole sine wave. In Fig. 5(c), the channels of the CMR are interrelated, and the current passing through each channel is no longer a simple sine wave, but an envelope composed of its maximum current.

In addition to the analysis of each channel waveform described previously, the current gain from the receiver to the load is plotted in combination with the information in Table I, as shown in Fig. 6. When the number of channels is 2, the CMR and PCDR have the same topology and the current gain is the same. With the number of channels increases, the growth rate of the CMR is significantly faster than that of the PCDR.

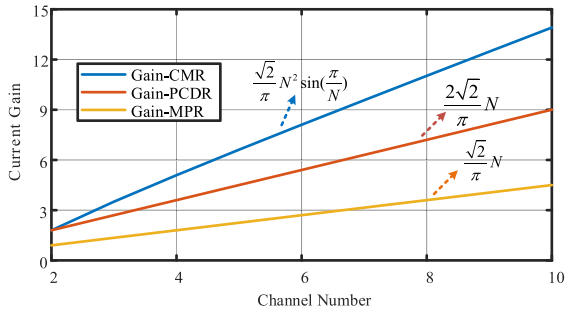

Fig. 6. Comparison of current gains of CMR, PCDR, and MPR systems.

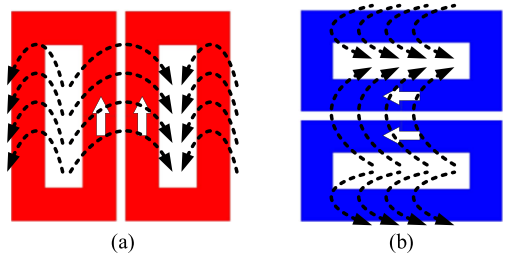

Fig. 7. Typical DD coil structure. (a) Direction I. (b) Direction II.

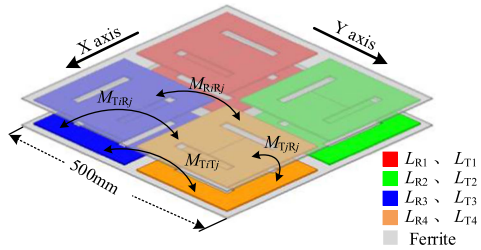

Fig. 8. Proposed four-channel WPT couplers.

III. DESIGN OF THE MAGNETIC COUPLER

The typical DD coils of the WPT system have two main types of placements, as shown in Fig. 7. It shows that both types of coils generate a magnetic field perpendicular to the direction of placement. For DD coils with different placement directions, the magnetic flux is symmetrical, and the positive inflow magnetic flux is equal to the negative inflow magnetic flux. Therefore, the net magnetic flux is 0, the mutual inductance is also 0, and the coils are decoupled from each other.

To ensure that each channel transmit power evenly without energy coupling, a perpendicular DD coil array structure is designed based on the aforementioned coil decoupling method, in which adjacent coils are consistent and rotated 90° to achieve consistent mutual inductance without cross coupling. Taking the four-channel WPT system as an example, the couplers are shown in Fig. 8. It contains eight coils, namely $L_{\mathrm{T}i}$ and $L_{\mathrm{R}i}$ ($1 \leq i \neq j \leq 4$). The mutual inductance between $L_{\mathrm{T}i}$ and $L_{\mathrm{R}i}$ are defined as $M_{\mathrm{T}i\mathrm{R}j}$, and the mutual inductance between $L_{\mathrm{T}i}$ ($L_{\mathrm{R}i}$) and $L_{\mathrm{T}j}$ ($L_{\mathrm{R}j}$) are defined as $M_{\mathrm{T}i\mathrm{T}j}$ ($M_{\mathrm{R}i\mathrm{R}j}$).

To verify the performance of the structure shown in Fig. 8, a simulation model is established in which the ferrite size is 500 mm × 500 mm and air gap is 70 mm. The mutual inductance between L_{T1} and other coils is shown in Fig. 9 as the number of

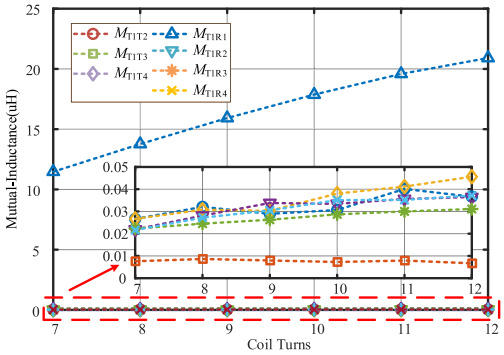

Fig. 9. Mutual inductance variation with coil turns.

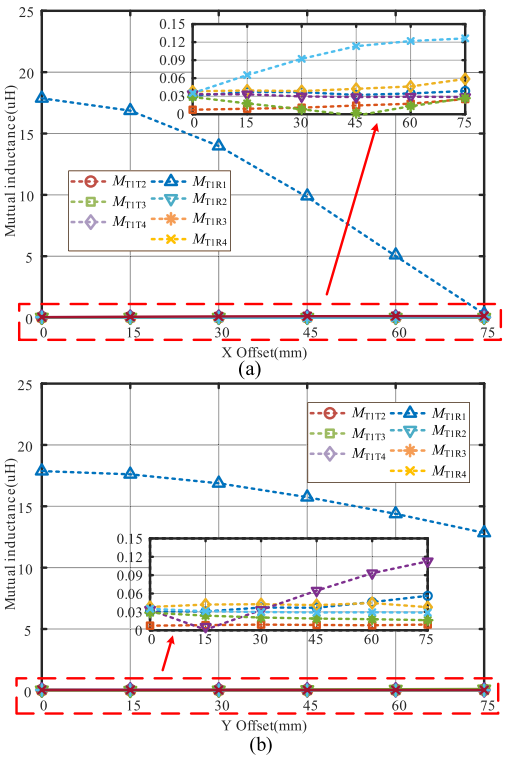

Fig. 10. Mutual inductance variation with offset. (a) X-axis. (b) Y-axis.

turns change. The mutual inductance increases with the increase of the number of turns, but the cross-mutual inductance grows slowly, and the amplitude is small compared with M_{T1R1}.

Fig. 10 shows the mutual inductance change when the coil is offset in the *X*- or *Y*-direction. The mutual inductance M_{T1R1} decreases with the increase of offset, while the cross inductance is always small. When offsetting to 75 mm in the *X*-direction, the mutual inductance M_{T1R1} drops to 0, while the mutual inductance offset along the Y-axis decreases by only about 1/3. This is because the positive inflow magnetic flux decreases when moving in the *Y*-direction, and the net magnetic flux decreases as it moves along the *X*-axis, except that the positive inflow magnetic flux decreases and the negative inflow magnetic flux begins to increase, the net magnetic flux and mutual inductance decrease faster.

In addition, the proposed coupling structure also has the characteristics of flexible expansion of the number of channels,

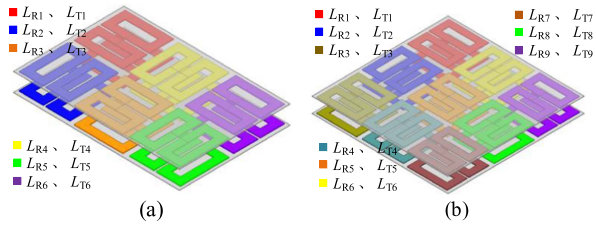

Fig. 11. Proposed WPT couplers. (a) Six-channel. (b) Nine-channel.

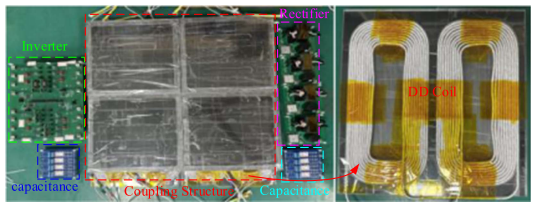

Fig. 12. Experimental platform of the proposed system.

TABLE II
PARAMETERS OF EXPERIMENTAL PROTOTYPE

V_{INV}	140 V	f	85 kHz	R_{L}	1.2 Ω	d	70 mm
L_{T1}	72.8 μH	L_{R1}	72.1 μH	M_{T1R1}	14.1 μH	C_{T1}	48.2 nF
L_{T2}	70.6 μH	L_{R2}	73.1 μH	M_{T2R2}	13.5 μH	C_{T2}	49.7 nF
L_{T3}	73.0 μH	L_{R3}	72.5 μH	M_{T3R3}	13.9 μH	C_{T3}	48.1 nF
L_{T4}	72.0 μH	L_{R4}	73.2 μH	M_{T4R4}	13.6 μH	C_{T4}	48.7 nF
C_{R1}	49.6 nF	L_{11}	241 μH	L_{12}	241 μH	M_1	240 μH
C_{R2}	47.9 nF	L_{21}	197 μH	L_{22}	197 μH	M_2	195 μH
C_{R3}	48.4 nF	L_{31}	217 μH	L_{32}	217 μH	M_3	215 μH
C_{R4}	47.9 nF	L_{41}	231 μH	L_{42}	231 μH	M_4	229 μH

which can face different levels of current output requirements. Based on the four-channel system, the coupling structures of six-channel and nine-channel systems are modeled in Fig. 11(a) and (b). With the increase of the number of channels, the coils can be expanded individually in a single direction or in multiple directions at the same time under the premise of ensuring that the adjacent channel coils are perpendicular to each other, with a high degree of freedom.

As new channel being added, they can be added on the basis of the original without redesigning, and can be directly spliced and expanded between different channel systems, indicating that the coupling structure proposed in this article has high compatibility.

IV. Experimental Validation

A. Experimental Setup

To verify the effectiveness of the proposed topology, a 2-kW WPT system with 140-V input and 48-V output voltage is established, as shown in Fig. 12. The structure of coils is consistent with the design in Fig. 8. The main parameters of the system are shown in Table II.

B. Experimental Results

In Fig. 13, the waveforms of the inverter ($U_{\mathrm{T}i}$, $I_{\mathrm{T}i}$) are depicted. The current is still sinusoidal and the proposed *N*-channel CMR has no impact on the Tx circuit behavior. The difference is only 1/4 cycle from the adjacent channels. Meanwhile, the MOSFET of all channels can realize zero-voltage switching.

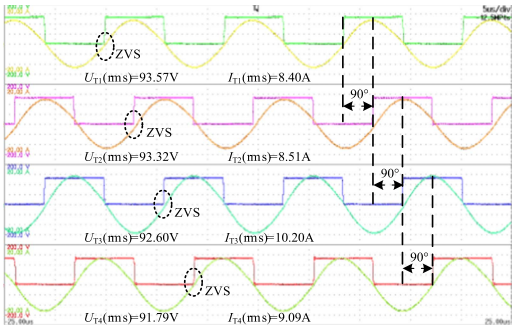

Fig. 13. Voltage and current waveforms of the inverter ($U_{\mathrm{T}i}$, $I_{\mathrm{T}i}$).

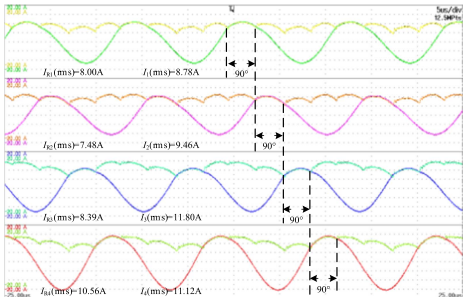

Fig. 14. Currents of the Rx coils and transformers ($\boldsymbol{I}_{\mathbf{R}i}$, I_i).

TABLE III
EXPERIMENTAL RESULTS WITH DIFFERENT OUTPUT POWER

Input Power	Output Power	Efficiency
2222.3 W	1951.3 W	87.8%
1058.4 W	926.2 W	87.5%
706.9 W	610.7 W	86.4%
617.5 W	522.3 W	84.6%

Fig. 14 shows the current of the Rx coils and transformers. The current flowing through each transformer is consistent, which is the envelope of Rx coil current and is composed of the part with the largest current on each channel. Each channel provides energy feedback output alternately, and each channel only provides 1/4 cycle energy.

Combined with the waveform under the rated power, it can be seen that the resonance relationship of the system has not changed, the current on Tx and Rx still maintains the sinusoidal waveform, and the current on the CMR is the peak envelope of the Rx current, which is consistent with the previous analysis. The waveforms between the channels are 90° different in phase, and the power transmission is independent of each other. In addition, different output power levels are also experimented with the constant output voltage. The input power, output power, and efficiency are shown in Table III.

V. CONCLUSION

Under the high-current requirement of different levels, an *N*-channel interleaved current-multiplier WPT systems is proposed in this article, which has the characteristics of high scalability, current gain, and system compatibility. By modeling and analyzing, the input characteristics of the *N*-channel CMR is consistent with the output characteristics of the S-S compensation network when expand, and can be directly connected in practical applications. The coupling structure adopts perpendicular DD coil array structure, which not only avoids the influence of cross inductance on the system, but also ensures the consistency of mutual inductance between facing coils and improves the stability of the system. The experiment results indicate that the 48-V 40-A output with the efficiency of 87.8% can be achieved. In the expansion, the required devices for each channel can be added directly on this system without the need for redesign.

REFERENCES

[1] Y. Zhang et al., "High-current output for AGV wireless charging system with intertwined receiving coils and split compensating capacitors," *IEEE Trans. Power Electron.*, vol. 40, no. 7, pp. 8923–8927, Jul. 2025.
[2] Y. Wu et al., "An integrated charger of wireless power transfer, onboard charger, and auxiliary power module for electric vehicles," *IEEE Trans. Power Electron.*, vol. 40, no. 4, pp. 6334–6344, Apr. 2025.
[3] Z. Yan et al., "An underwater wireless power transfer system with improved misalignment tolerance," *IEEE J. Emerg. Sel. Topics Power Electron.*, vol. 13, no. 4, pp. 4369–4376, Aug. 2025, doi: 10.1109/JESTPE.2025.3541289.
[4] C. Cai et al., "Robust wide-area wireless charging of multipath movable receivers: A coupling mechanism and simplified configuration strategy," *IEEE Trans. Power Electron.*, vol. 40, no. 1, pp. 2527–2541, Jan. 2025.
[5] X. Yu et al., "Compact wireless power transfer with enhanced misalignment tolerance via independent secondary PWM control," *IEEE Trans. Power Electron.*, vol. 40, no. 9, pp. 11998–12002, Sep. 2025.
[6] H. Wang et al., "Blind-zone-free metal object detection system for wireless EV charging system employing strip multipolar detection coils," *IEEE Trans. Transp. Electrific.*, vol. 11, no. 1, pp. 4420–4428, Feb. 2025.
[7] W. Chen, J. Jia, X. Yan, Y. Song, and J. Li, "Wireless power supply based on MNG-MNZ metamaterial for cardiac pacemakers," *CES Trans. Elect. Machines Syst.*, vol. 8, no. 1, pp. 103–112, Mar. 2024.
[8] C. Liu, M. Zhou, R. Xie, X. Chen, X. Mao, and Y. Zhang, "An interoperable receiver with reconfigurable LCC compensation for wireless charging of 400- and 800-V batteries in electric vehicles," *IEEE Trans. Ind. Electron.*, vol. 72, no. 8, pp. 8710–8714, Aug. 2025.
[9] F. Lu et al., "A tightly coupled inductive power transfer system for low-voltage and high-current charging of automatic guided vehicles," *IEEE Trans. Ind. Electron.*, vol. 66, no. 9, pp. 6867–6875, Sep. 2019.
[10] Y. Liu, Y. Li, J. Xu, S. Liu, J. Liu, and Z. He, "A constant current output method for low-voltage and high-current DWPT systems based on inverse coupled current doubler rectifier," *IEEE Trans. Power Electron.*, vol. 39, no. 8, pp. 9113–9119, Aug. 2024.
[11] X. Li et al., "A high-efficiency IPT system with series-capacitor full-bridge configuration and inverse coupled current doubler rectifier for high-input, low-voltage, and high output current applications," *IEEE Trans. Power Electron.*, vol. 39, no. 9, pp. 11849–11861, Sep. 2024.
[12] Y. Li, J. Chen, Y. Liu, X. Zhao, M. Fu, and Z. He, "An accurate modeling and suppression method for current imbalance in dual-receiver WPT systems for low-voltage and high-current applications," *IEEE Trans. Transp. Electrific.*, vol. 10, no. 3, pp. 7065–7075, Sep. 2024.
[13] L. Yang, K. Dong, Y. Wang, C. Cai, and X. Zhou, "Analysis, design, and validation of a dual-channel high-power WPT system based on bilateral coil decoupling," *IEEE J. Emerg. Sel. Topics Power Electron.*, vol. 12, no. 4, pp. 4288–4295, Aug. 2024.
[14] Y. Wang, S. Zhao, R. Kheirollahi, A. Mostafa, H. Zhang, and F. Lu, "Multiphase interleaved IPT based current-source converter for high-current application," *IEEE J. Emerg. Sel. Topics Ind. Electron.*, vol. 3, no. 3, pp. 583–593, Jul. 2022.
[15] Q. Deng, X. Wang, J. Chen, X. Gao, P. Luo, and L. Wang, "A self-balanced multi-channel wireless charging system for EV," *IEEE Trans. Veh. Technol.*, vol. 73, no. 11, pp. 16491–16502, Nov. 2024.
[16] C. Tao, Z. Liu, S. Li, Y. Guo, and L. Wang, "A high-efficiency wireless power transfer system using quasi-Z-source inverter and current-double synchronous rectifier for low-voltage and high-current applications," *IEEE Trans. Transp. Electrific.*, vol. 8, no. 2, pp. 2758–2769, Jun. 2022.
[17] L. Shi, A. Delgado, R. Ramos, and P. Alou, "A wireless power transfer system with inverse coupled current doubler rectifier for high-output current applications," *IEEE Trans. Ind. Electron.*, vol. 69, no. 5, pp. 4607–4616, May 2022.